Radio-frequency ablation electrode displacement elastography: A phantom study

Shyam Bharat and Tomy Varghese[a)]
Department of Medical Physics and Department of Electrical and Computer Engineering, University of Wisconsin—Madison, 1300 University Avenue, 1530 MSC, Madison, Wisconsin 53706

Ernest L. Madsen and James A. Zagzebski
Department of Medical Physics, University of Wisconsin—Madison, 1300 University Avenue, 1530 MSC, Madison, Wisconsin 53706

(Received 6 September 2007; revised 9 April 2008; accepted for publication 9 April 2008; published 22 May 2008)

This article describes the evaluation of a novel method of tissue displacement for use in the elastographic visualization of radio-frequency (rf) ablation-induced lesions. The method involves use of the radio-frequency ablation electrode as a displacement device, which provides localized compression in the region of interest. This displacement mechanism offers the advantage of easy *in vivo* implementation since problems such as excessive lateral and elevational displacements present when using external compression are reduced with this approach. The method was tested on a single-inclusion tissue-mimicking phantom containing a radio-frequency ablation electrode rigidly attached to the inclusion center. Full-frame rf echo signals were acquired from the phantom before and after electrode displacements ranging from 0.05 to 0.2 mm. One-dimensional cross-correlation analysis between pre-and postcompression signals was used to measure tissue displacements, and strains were determined by computing the gradient of the displacement. The strain contrast, contrast-to-noise ratio, and signal-to-noise ratio were estimated from the resulting strain images. Comparisons are drawn between the elastographically measured dimensions and those known *a priori* for the single-inclusion phantom. Electrode displacement elastography was found to slightly underestimate the inclusion dimensions. The method was also tested on a second tissue-mimicking phantom and on *in vitro* rf-ablated lesions in canine liver tissue. The results validate previous *in vivo* findings that electrode displacement elastography is an effective method for monitoring rf ablation. © *2008 American Association of Physicists in Medicine*.
[DOI: 10.1118/1.2919763]

Key words: ablation, compression, displacement, elastography, elastogram, elasticity, elasticity imaging, electrode displacement, radio-frequency ablation, strain, ultrasound

I. INTRODUCTION

Imaging of tissue elastic parameters for diagnosis of disease is rapidly gaining attention because of the ability to provide noninvasive and new information.[1–26] Tissue elasticity imaging methods based on ultrasound fall into three main groups: (1) Methods that include elastography, where a quasistatic compression is applied and the resulting components of the strain tensor are estimated;[5–10,27] (2) methods where a low-frequency vibration is applied, with ultrasound Doppler detection of velocities of perturbed reflectors;[2–4] and (3) methods that use acoustic radiation force.[28–32] RF ablation produces protein denaturation due to temperature elevation, inducing an increase of the elastic modulus of soft tissue. With elasticity imaging techniques, these changes appear as regions that incur less strain upon displacement than surrounding untreated tissue.[33–35]

Elastography generally produces images of tissue strains resulting from external quasistatic compression.[5,6] A strain image, or elastogram, is a map of local strain incurred in tissue due to this quasistatic compression. The effectiveness of the resulting elastogram in depicting the underlying strain is highly dependent on the efficiency of the compression mechanism and the synchronization of the data acquisition with the compression.[5] It has been shown previously that elastograms with high signal-to-noise ratio (SNR_e) and contrast-to-noise ratio (CNR_e) can be obtained using an external compressor plate to provide uniform tissue compression.[5,36] The external compression technique is feasible for superficial tissue such as the breast and thyroid. However, it is difficult to implement this method of compression for internal organs such as the liver or kidney because the resultant poor coupling would lead to nonuniform compression, which in turn would culminate in elastograms with low SNR_e and CNR_e. In addition, problems such as excessive lateral and elevational motion are also present with the external plate compression technique.[37]

One of the applications of elastographic imaging is in monitoring the size and extent of coagulated regions created using ablative therapies.[37–40] The focus in this article is on rf ablation, a procedure where an electrode is placed in the targeted area of tissue and a 450 KHz rf current is delivered to the region. Ionic agitation in the tissue area adjacent to the electrically active region of the electrode causes intense heating in a localized region of tissue.[41,42] Ablation temperatures

greater than 42 °C are known to be lethal, depending on the ablation duration,[43,44] while ablation temperatures of 60 °C and higher lead to instant tissue necrosis.[45] Conventional ultrasound has been used to monitor lesion extent in rf ablation procedures,[45–47] but it suffers from poor contrast between treated and untreated regions.[41,48] In contrast, the ablated region is known to be significantly stiffer than the surrounding nonablated tissue due to the process of protein denaturation that occurs at the high temperatures encountered in rf ablation.[34,37,39,40] Similar results have also been reported for tissue ablation using high-intensity focused ultrasound.[49] Thus, ablated regions are discernible on strain images because of their higher stiffness compared to untreated regions.

External compression elastography generally is not practical for monitoring ablation therapy in most *in vivo* abdominal sites of interest due to limited access for a compression plate or for compressions using the transducer itself. However, Varghese *et al.*[37] have shown for *in vivo* elastographic monitoring of thermal lesions created by rf ablation that tissue displacements can be achieved using perturbations of the rf ablation electrode as the mechanical stimulus. This idea of localized compression was also utilized by Nightingale *et al.* using acoustic radiation force to introduce perturbations in the targeted region of tissue.[13] Following the initial work by Varghese, finite element simulations modeling the electrode displacement technique have also been carried out,[50] and show that the incremental displacements applied to the electrode serve to provide localized compression in the region of interest, i.e., the thermal lesion. The areas of strain depicted by the finite element analysis model were in general agreement with patterns seen in the *in vivo* experiment.

This article describes a phantom-based evaluation of the electrode displacement method. The results presented here verify strain patterns seen in our previous reports; furthermore, they provide information about the inclusion dimensions viewed on elastograms and how they compare with known dimensions. Other parameters presented include the strain contrast of the inclusion and noise properties characterized using the CNR_e and SNR_e.

II. MATERIALS AND METHODS

A custom tissue-mimicking (TM) "electrode displacement" phantom was constructed, a diagram of which is shown in Fig. 1. The TM materials in the phantom[51] consist of dispersions of microscopic safflower oil droplets in a gelatin matrix. A 19 mm diameter spherical inclusion was formed around the hooked end of a stainless-steel rod, the latter representing an ablation electrode. The inclusion is bonded to the hooked tip of the rod. A storage modulus (real part of the complex Young's modulus) of 50 ± 2 kPa was measured at 1 Hz for the inclusion material using a Bose EnduraTEC® model ELF 3200 system.[52] Surrounding the inclusion and bonded to it is the background material with a storage modulus of 11 ± 2 kPa. Thus, the inclusion is approximately 5 times stiffer than the background. These modulus contrast values were selected based on information published in the peer-reviewed literature.[53,54] Oil droplets in both materials

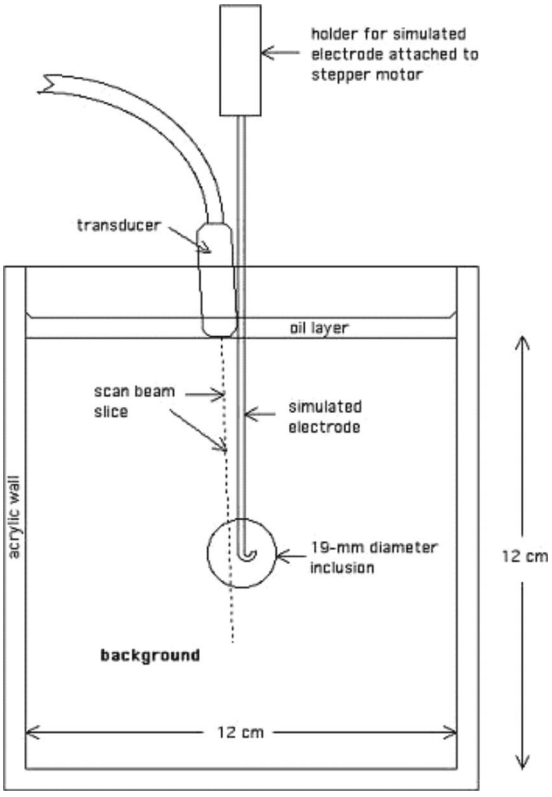

FIG. 1. Experimental setup showing the single-spherical inclusion phantom with an electrode embedded in the inclusion. Inclusion displacement for elastography is induced by applying precise, stepper motor controlled displacements to the upper unconstrained end of the electrode. Pre- and post-displacement raw rf data are collected using the ultrasound transducer positioned adjacent to the electrode.

provide tissuelike ultrasonic backscatter and attenuation. The inclusion is centered in the $12 \times 12 \times 12$ cm cube of background material. Note that the inclusion here represents the lesion after it is formed by rf ablation. In other words, the aim is to model the elastic properties of the lesion formed by rf ablation and not the ablation procedure itself.

To generate elastograms, the simulated electrode was displaced vertically using a stepper motor system, producing displacements in the range 0.05–0.2 mm. A real-time ultrasound scanner, an Aloka SSD 2000 (Aloka, Tokyo, Japan), was used for acquiring rf data. The transducer used was a linear array transducer having a center frequency of 5 MHz, a 40 mm footprint, and a 70% bandwidth. Digitization was performed using an external 12-bit data acquisition board (Gage, Montreal, QC, Canada) at a sampling rate of 100 MHz. Displacement estimates were obtained using 1D cross correlation, with a window length of 3 mm. 1D cross correlation was utilized because it was better suited to the electrode displacement method when compared to 2D cross correlation, which was insensitive to the small displacements encountered with electrode displacement elastography. The corresponding strains were calculated using a 5-point linear least-squares estimator.

Figure 1 provides a schematic diagram of the experimental setup. The ultrasound transducer was placed adjacent to the electrode, in a plane approximately parallel to that of the electrode (see the Appendix for details). Pre- and postdisplacement rf data were acquired for two different displacement conditions: (1) Displacement of the inclusion away from the ultrasound transducer, and (2) displacement of the inclusion toward the ultrasound transducer, the latter following an initial displacement of 0.25 mm away from the transducer. Ten independent data sets were acquired for each of four different displacement increments (0.05, 0.1, 0.15, and 0.2 mm), for both the above-mentioned data acquisition methods. Displacements greater than 0.2 mm were used to avoid physical damage to the phantom by the loss of contact between the rf electrode and the inclusion. In a real rf ablation experiment, there could be a similar "threshold" for the applied displacements, the crossing of which could result in a loss of contact between the electrically active region of the electrode and the lesion formed during the ablation procedure. The ten data sets were acquired by rotating the ultrasound transducer around the electrode and recording one data set for a particular orientation of the transducer with respect to the electrode, to obtain independent data sets.

The inclusion was expected to be visible as a low-strain region on the elastogram. In addition, since the displacements were applied to the electrode, which in turn was adhered to the inclusion, the strains developed in the phantom were expected to be more localized than, for example, those obtained using external compression elastography. Thus, we decided to perform an analysis to compare how effectively contrast is depicted on the elastograms corresponding to different values of displacement.

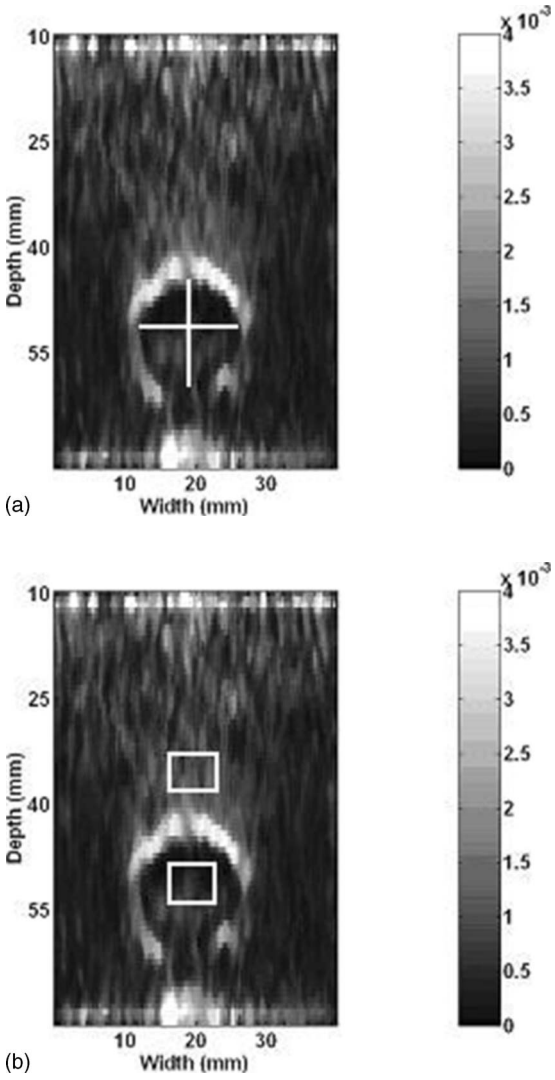

FIG. 2. (a) Computation of the width and height estimates on the electrode displacement elastograms. (b) Selection of the regions of interest (ROIs) on the elastograms for computation of the strain contrast, CNR_e and SNR_e. Pixels enclosed by the ROIs were considered for calculating these quantities.

II.A. Computation of width, height, and area estimates

Figure 2 presents a typical electrode displacement elastogram. The inclusion is seen as the central dark disk within a bright halo. In elastography, stiffer regions undergo lower strains and are depicted as dark regions on the elastograms. Figure 2(a) illustrates the method of calculation of the width and height of the elastographically depicted inclusion. These two parameters were manually estimated using two points on diametrically opposite sides of the inclusion. Points were selected along the horizontal or vertical axis and were chosen to lie on the boundary of the inclusion and the background, based on visual inspection. The area estimates were obtained using manual segmentation of the inclusion. A closed region along the inclusion boundaries was drawn, and the area enclosed by it was taken to be the area estimate of the inclusion. This method of area computation was followed to remove the dependence of the area estimates on the assumption of an elliptical model, previously used for lesion area calculations.[34] Note that the distal boundary of the inclusion is not clearly visible. This is believed to be a result of shadowing from the hooked end of the rf electrode. For height and area estimates, the distal boundary was extrapolated based on the rest of the inclusion boundary. The above computations were performed on the strain images from all ten data sets in an experiment and averaged to obtain a mean and standard deviation.

As can be seen in Fig. 1, the plane imaged by the ultrasound transducer is slightly off-center with respect to the electrode. As a result of this, the computed width, height, and area of the imaged plane of the inclusion are slightly less than the actual values. To correct for this discrepancy, we multiply the computed estimates of width, height and area by a correction factor (see the Appendix). The estimates, with the correction factor incorporated, were then compared to the known inclusion diameter and area.

II.B. Computation of strain contrast, CNR_e, and SNR_e

Two rectangular regions of interest (ROIs), one within the inclusion and one above the inclusion (in the background), were used in the computation of the strain contrast, CNR_e

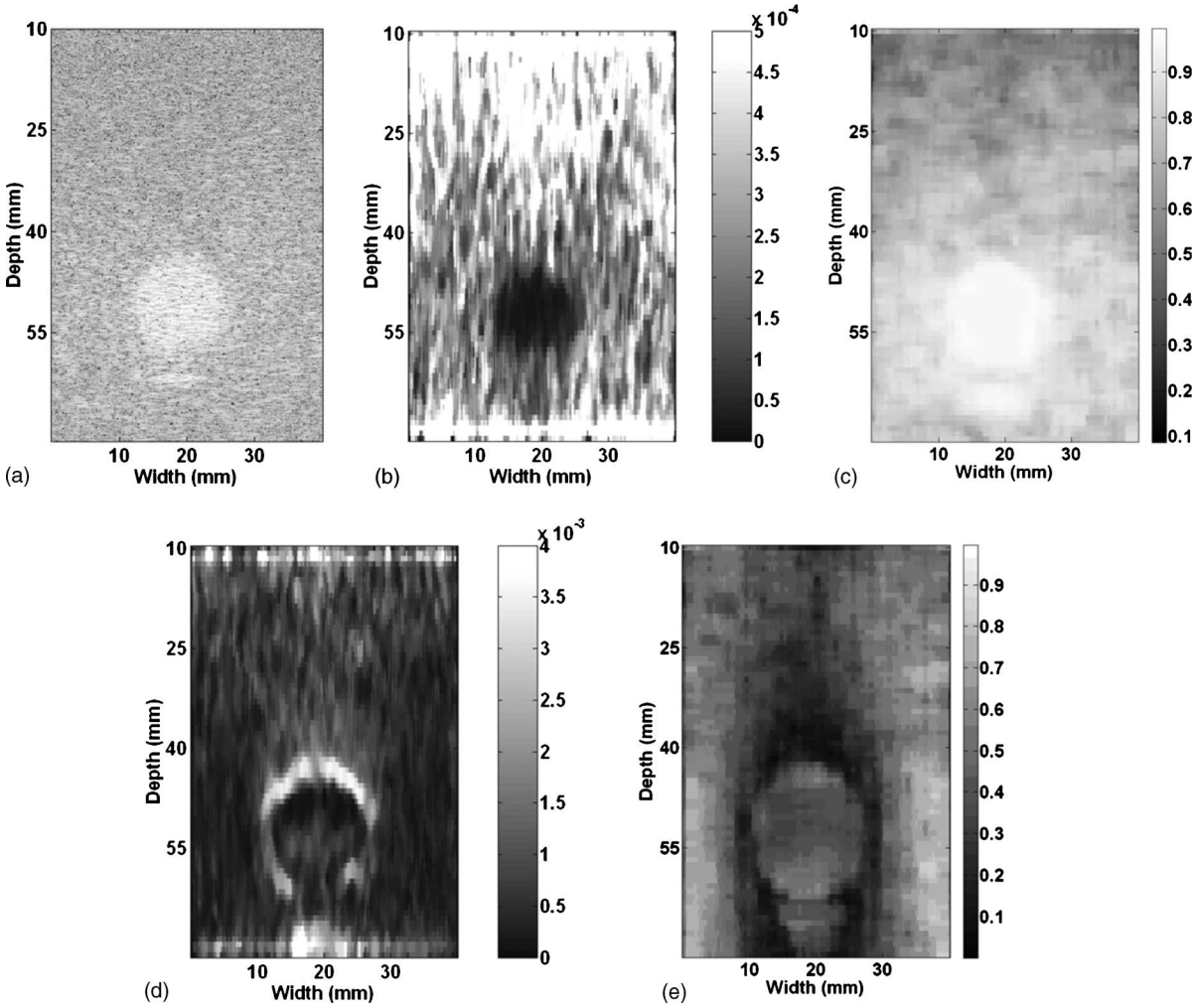

FIG. 3. Images resulting from different stages of inclusion displacement away from the ultrasound transducer. (a) B-mode image of the phantom. (b) Elastogram corresponding to a displacement of 0.05 mm. (c) Correlation coefficient image for the elastogram in (b). (d) Elastogram corresponding to a displacement of 0.2 mm. (e) Correlation coefficient image for the elastogram in (d).

and SNR_e. Figure 2(b) illustrates the selection of the two ROIs for the computation of these quantities. The strain contrast was computed using the following formula:[55]

$$\text{Strain contrast} = \frac{s_1}{s_2}, \tag{1}$$

where s_1 and s_2 are the mean pixel values of the ROI in the background and the inclusion, respectively. The strain contrast was calculated in the manner shown above in order to facilitate direct comparison between elastographically measured contrast and the known modulus contrast of the inclusion. An important characteristic of the electrode displacement method is the localized nature of the displacements. As observed in Fig. 2, the local strains or displacements to the right and left of the inclusion are very small. We did not choose our background ROI to lie in these regions of low strain, as they would not then accurately represent the background strain. This left the regions above and below the inclusion as possible locations for the background ROI. The region for the ROI in the background was selected slightly above the inclusion, as illustrated in Fig. 2(b). However, a similar region can also be selected below the inclusion. The other parameter to be selected was the position of the background ROI above the inclusion. We chose the background ROI to be as close to the inclusion as possible, while avoiding the regions of high strain values just above the inclusion. Since these regions have increased strain, they could suffer from increased decorrelation resulting from higher (or possibly lateral) displacements that could not be tracked by the algorithm. The reason for choosing a location near the inclusion for the background ROI is that visual contrast demarcation is generally made by the human eye for regions located close to each other.

The CNR_e is an important indicator of the ease with which the inclusion can be detected.[56] Higher values of CNR_e imply easier inclusion detectability. The following expression is used to calculate the CNR_e:

$$\text{CNR}_e = \frac{2(s_1 - s_2)^2}{\sigma_{s_1}^2 + \sigma_{s_2}^2}, \tag{2}$$

where s_1 and s_2 are the mean pixel values defined above, and σ_{s1} and σ_{s2} are the standard deviations of the ROI in the

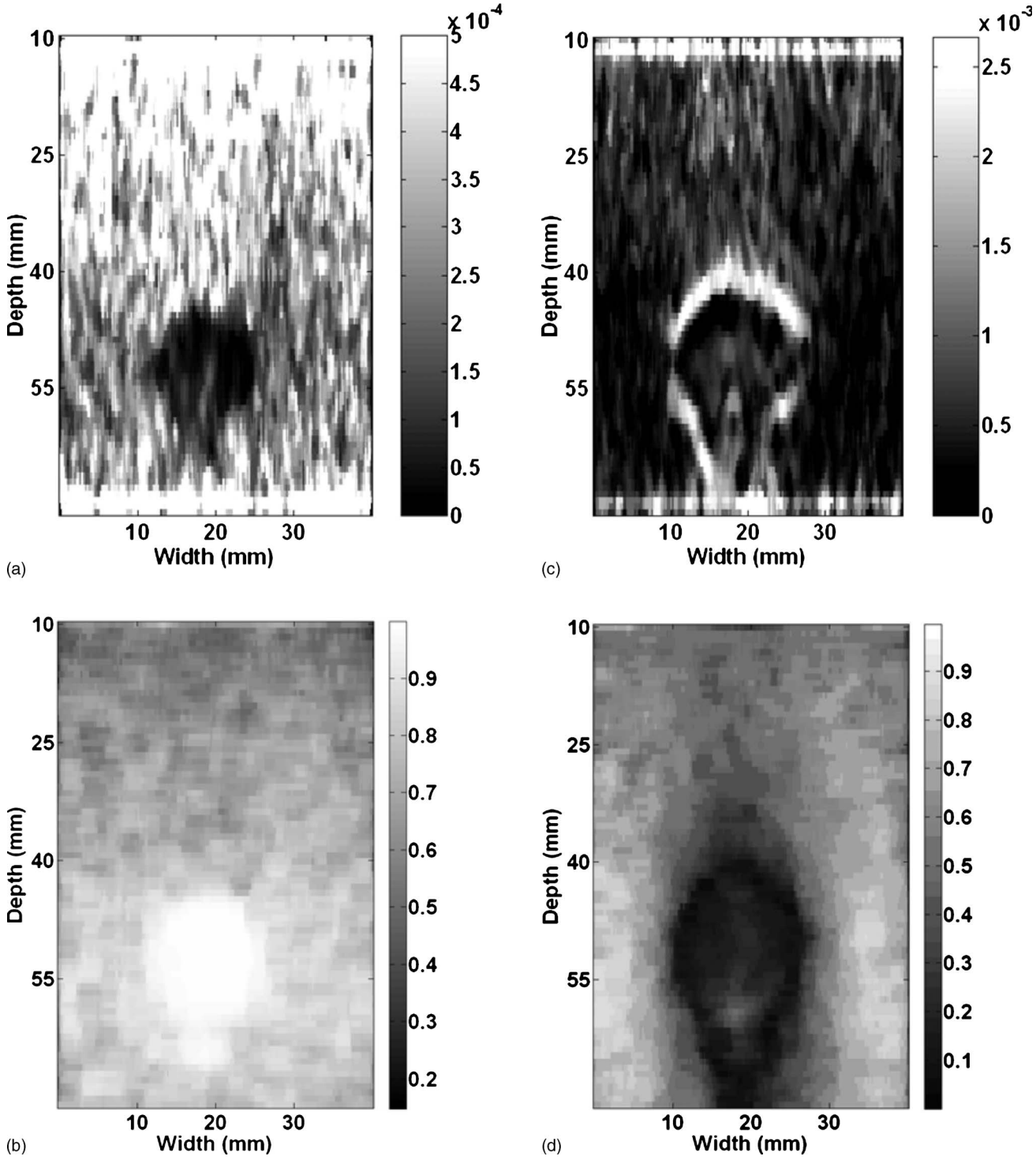

FIG. 4. Elastograms resulting from different stages of inclusion displacement toward the ultrasound transducer. (a) Elastogram corresponding to a displacement of 0.05 mm toward the ultrasound transducer, after an initial displacement of 0.25 mm away from the transducer. (b) Correlation coefficient image for the elastogram in (a). (c) Elastogram corresponding to a displacement of 0.2 mm toward the ultrasound transducer, after an initial displacement of 0.25 mm away from the transducer. (d) Correlation coefficient image for the elastogram in (c).

background and the inclusion, respectively. In the calculations for strain contrast and CNR_e, the average mean pixel value and standard deviation for the background ROI were used for all calculations at a particular displacement level. As a result, the trends observed in these parameters for different displacements can solely be attributed to the characteristics of the inclusion on the elastogram.

The SNR_e of the inclusion is given by the ratio of the mean pixel value to its standard deviation for pixels enclosed by the ROI within the inclusion.[57] Thus,

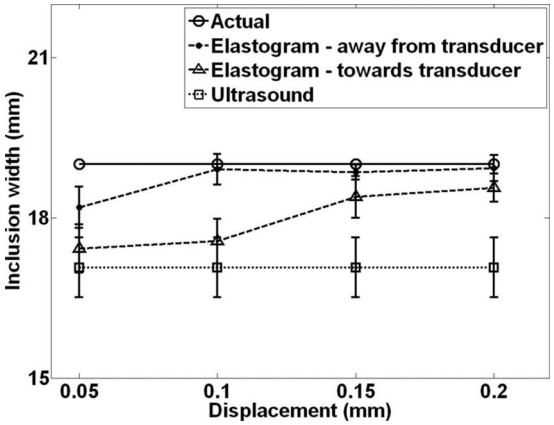

FIG. 5. Comparison of elastographic and B-mode estimates of inclusion width with its actual value, in case of inclusion displacement away from and toward the ultrasound transducer. The error bars represent standard error, which is the standard deviation divided by the square root of the number of experiments.

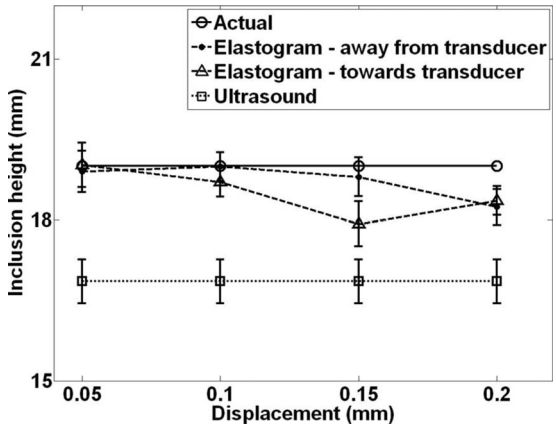

FIG. 6. Comparison of elastographic and B-mode estimates of inclusion height with its actual value, in case of inclusion displacement away from and toward the ultrasound transducer. The error bars represent standard error, which is the standard deviation divided by the square root of the number of experiments.

$$\mathrm{SNR}_e = \frac{s_2}{\sigma_{s_2}}, \tag{3}$$

where s_2 and σ_{s_2} are as defined above.

II.C. Additional TM phantom and *in vitro* validation

The electrode displacement method was also evaluated on a second TM phantom to verify the repeatability of the method. The composition of this TM phantom is similar to the one described earlier, the main differences being the shape of the electrode and the storage moduli of the inclusion and background. The electrode in this case is a single straight rod, without the hooked end as in the previous phantom. Single electrodes are commonly used in clinical rf ablation procedures. The storage modulus of the background was measured to be 13.5 ± 2 kPa at 1 Hz, while that of the inclusion was measured to be 54 ± 2 kPa, also at 1 Hz. Thus, the modulus contrast for this phantom is approximately 4:1.[53,54]

In addition to testing on the second TM phantom, the method was also evaluated on canine liver tissue *in vitro*, after creation of a rf-ablated thermal lesion in the liver. The rf ablation procedure was performed on excised canine liver using a Valleylab Cool-tip™ ablation electrode (Valleylab, CO). The electrode used was a 17-gauge single electrode, with a 2–3 cm long electrically active region at the tip that is embedded in tissue. After the rf ablation procedure, the liver with the attached rf electrode was encased in a cubic block of gelatin for performing electrode displacement elastography. For the *in vitro* testing, we used a Siemens C7F2 4D curvilinear ultrasound transducer at a center frequency of 4.4 MHz (Siemens Medical Solutions, USA, Inc., Issaquah, WA) for data acquisition.

III. RESULTS

Figure 3(a) presents an ultrasound B-mode image of the inclusion, while Figs. 3(b) and 3(d) show the elastograms resulting from displacements of 0.05 and 0.2 mm, respectively, away from the ultrasound transducer. Figures 3(c) and 3(e) depict images of the correlation coefficient for displacements of 0.05 and 0.2 mm, respectively, away from the transducer. Figure 4 shows corresponding images for displacements of 0.05 and 0.2 mm, respectively, only with the displacement toward the imaging transducer. The elastograms display a halo or bright region around the inclusion for displacements greater than 0.05 mm. This halo, probably due to increased local displacement gradients, is restricted to regions around the inclusion and is tracked on the rf pre- and postdisplacement echo signals. In the correlation coefficient images, brighter pixels correspond to regions that are well-tracked by the algorithm, while darker pixels are indicative of increased signal decorrelation.

Differences in the strain images using the two displacement modes (toward and away from the transducer) are quantified using comparisons of the inclusion width, height, and area between the elastograms and the known values for the inclusion. Comparison between elastographically measured dimensions of the inclusion and the known inclusion dimensions provides useful information related to the accuracy of the electrode displacement method. Figure 5 shows comparisons between the actual width of the inclusion (i.e., diameter) and the inclusion width as seen on the strain images. Width estimates from B-mode images are also plotted. Note that the elastographic inclusion width estimates are close to the actual inclusion diameter at all displacement levels.

Figure 6, in a similar manner, presents comparisons between the elastographic and B-mode height estimates of the inclusion, with the known inclusion diameter. The elastograms generated provide reliable estimates of the inclusion height. Finally, Fig. 7 compares the known and elastographically estimated inclusion areas. Also shown are area estimates from B-mode images. The inclusion area appears to be underestimated on the elastograms. This underestimation could be a result of errors in the manual segmentation pro-

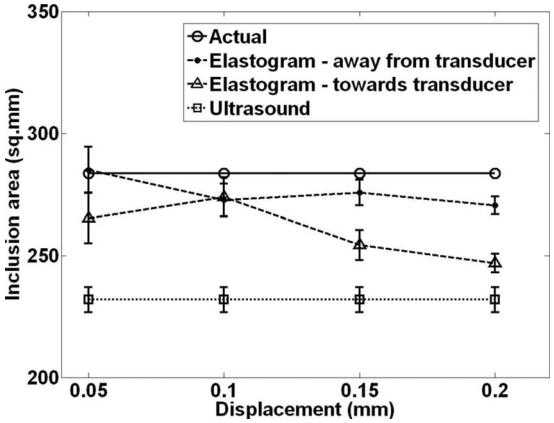

FIG. 7. Comparison of elastographic and B-mode estimates of inclusion area with its actual value, in case of inclusion displacement away from and toward the ultrasound transducer. The error bars represent standard error, which is the standard deviation divided by the square root of the number of experiments.

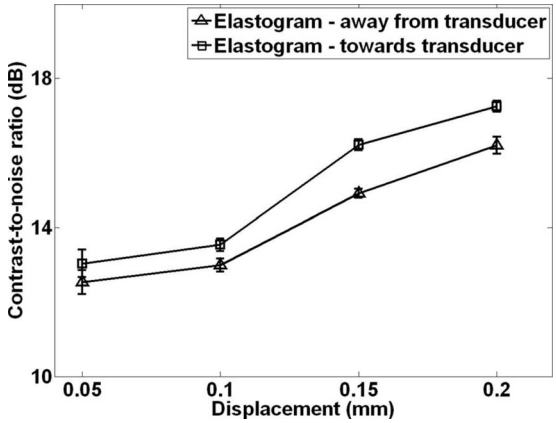

FIG. 9. Elastographic CNR_e vs displacements, for inclusion displacement away from and toward the ultrasound transducer. The error bars represent standard error.

cess. Also, the slight underestimation in both the height and width are manifested in a combined manner in the computation of area estimates.

Quantitative comparisons of the strain contrast, CNR_e and SNR_e, were also performed. Figure 8 presents plots of the elastographically computed strain contrast at different values of the electrode displacement. Observe that the strain contrast is consistently greater than the actual modulus contrast, both in the case of inclusion displacement away from the transducer and toward the transducer. Figure 9 illustrates the variation in the CNR_e values at different displacements. For both directions of inclusion displacement, the CNR_e values under all the observed displacements are consistent. Finally, Fig. 10 demonstrates trends seen in the SNR_e of the inclusion under different displacement levels. From these plots, the SNR_e values are found to be consistent under both experimental conditions studied (i.e., both directions of inclusion displacement). SNR_e values at different displacement levels are also comparable.

Corresponding B-mode, elastogram, and correlation coefficient images from data acquired from the second TM phantom are shown in Fig. 11. Figure 11(a) shows the B-mode image of the inclusion, while Figs. 11(b) and 11(c) display the elastogram and the correlation coefficient image, respectively. Similar to the first phantom, the inclusion is visible as a low-strain region surrounded by a halo. The correlation coefficient images also denote that the region with the halo corresponds to lower correlation coefficient values due to the increased strain and subsequent signal decorrelation.

Finally, Fig. 12 presents results obtained from performing electrode displacement elastography on thermal lesions created by performing rf ablation on canine liver tissue *in vitro*. Figure 12(a) shows the B-mode image of the lesion, while Fig. 12(b) shows the elastogram. Clear boundary delineation of the lesion is seen in the elastogram; however, the lesion cannot be demarcated on the B-mode image. Figure 12(c), where the elastographic boundaries of the lesion are traced onto the B-mode image, illustrates the fact that elastography can provide useful information complementary to that available from conventional ultrasound.

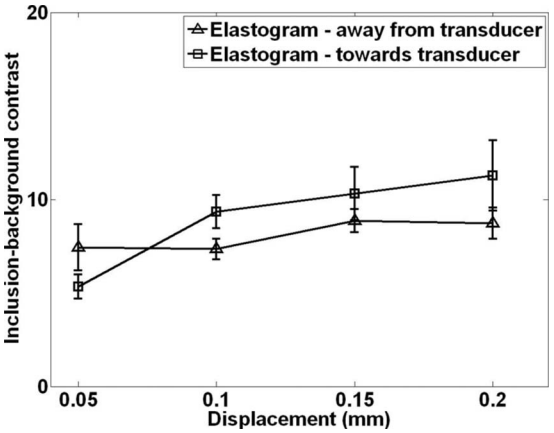

FIG. 8. Strain contrast on elastograms vs displacements, for inclusion displacement away from and toward the ultrasound transducer. The error bars represent standard error.

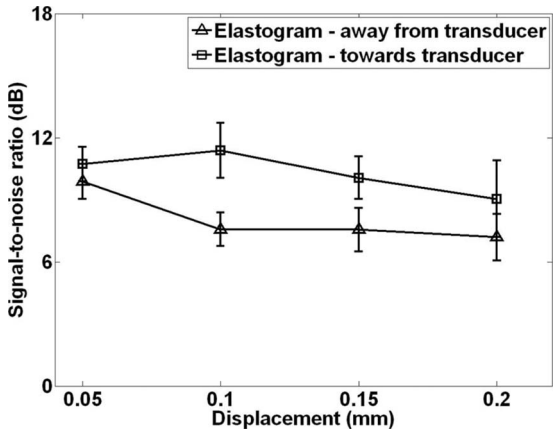

FIG. 10. Elastographic SNR_e vs displacements, for inclusion displacement away from and toward the ultrasound transducer. The error bars represent standard error.

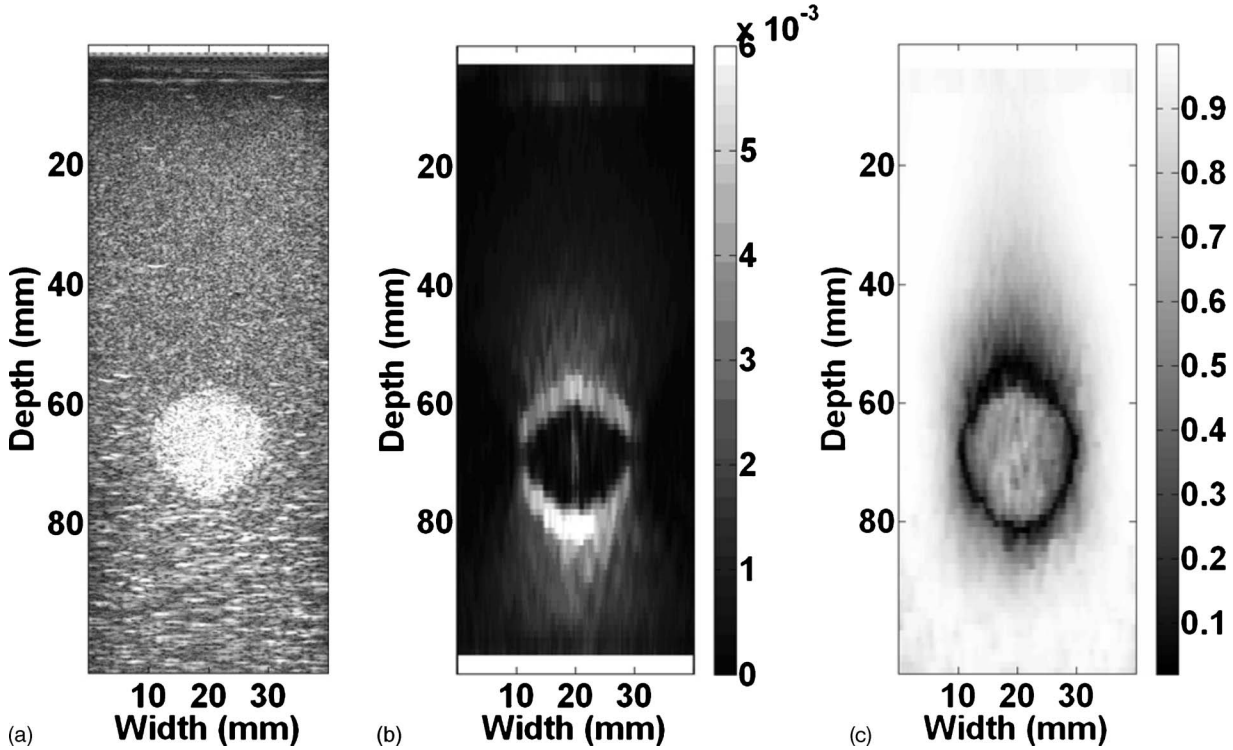

FIG. 11. Images from the second TM phantom. (a) B-mode image of the phantom. (b) Elastogram. (c) Correlation coefficient image.

IV. DISCUSSION AND CONCLUSIONS

Electrode displacement elastography of thermal lesions was evaluated using two specially constructed TM phantoms, each containing an inclusion attached to an ablation electrode. Two different electrode displacement approaches, where the inclusion was displaced toward and away from the transducer were evaluated. The elastographic inclusion size estimates were compared with the known inclusion diameter. In addition, quantitative parameters such as strain contrast, CNR_e, and SNR_e were estimated and compared for different displacement increments.

A correction factor was incorporated into the estimates of the inclusion dimensions on the elastograms to account for the fact that the imaged plane was slightly off-center with respect to the electrode. As a result of this off-center imaging plane, the maximum inclusion width and height were not fully visualized on the elastograms. After incorporating the correction factor, the resulting elastographic estimates were within 9% of the known inclusion diameter. Even after incorporation of the correction factor, there was a slight tendency for size and area underestimation on the elastograms. Variations in the width and height estimates have a combined effect on the area estimates. Dimensions calculated from B-mode images are also included to provide an additional yardstick for comparison. Note that the B-mode dimension estimates are independent of the magnitude of the displacement. Also, the inclusion has been made to appear hyperechoic on the B-mode image to aid in easy localization during rf data acquisition for electrode displacement elastography. Actual rf-ablated lesions may appear hyperechoic, isoechoic, or hypoechoic.[34] Hence, while we have compared inclusion dimension estimates from elastograms and B-mode images, this may not be possible in actual ablation experiments. The ultrasound contrast in our TM phantom is therefore not necessarily indicative of the contrast encountered in actual rf-ablated tissue. It is well-known that the depiction of rf-ablated lesions on B-mode images is generally not accurate.[46] This fact is evidenced from the B-mode image of the rf-ablated lesion, shown in Fig. 12(a).

The elastographically measured strain contrast was also compared to the known modulus contrast of the inclusion. Under all experimental conditions, the strain contrast obtained was significantly higher than the modulus contrast (which was approximately 5). Note that the comparison of the modulus contrast to the strain contrast in this article does not incorporate the contrast-transfer efficiency formulation used for external compression elastography. This elevation in the strain contrast could be a result of the local perturbation method used for electrode displacement elastography. In addition, the signal decorrelation artifacts observed around the inclusion may contribute to an elevation in the strain contrast values if the regions of interest are placed in these areas. However, the increased decorrelation around the inclusion actually serves to delineate the inclusion from the background and aids in the visual demarcation of the inclusion.

The CNR_e for both directions of displacement tends to increase marginally with the amount of displacement. The CNR_e being an indicator of inclusion detectability, it is concluded that inclusions depicted on elastograms corresponding to higher displacements are more easily detectable than

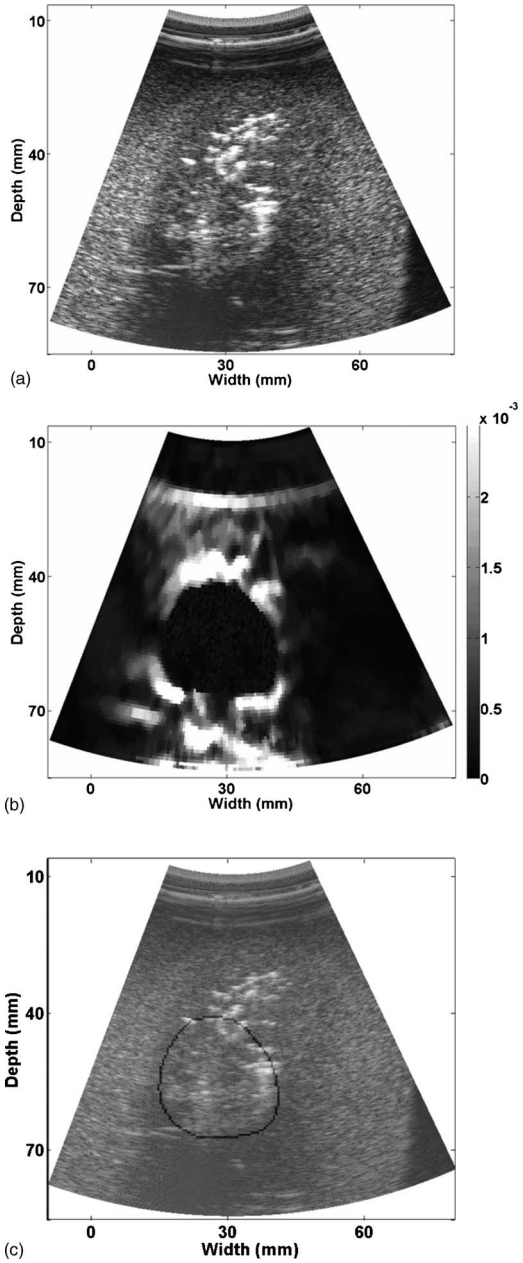

FIG. 12. Images from the *in vitro* rf ablation experiment. (a) B-mode image of the rf-ablated lesion. (b) Elastogram. (c) Overlay of the lesion boundaries from the elastogram on the B-mode image. The elastogram in (b) depicts the lesion as a dark region with regular boundaries surrounded by a bright halo. The lesion, however, is not clearly visible in the B-mode image in (a), as shown by comparison with the elastographic lesion boundaries in (c).

those depicted on elastograms corresponding to lower displacements. The CNR_e values shown in Fig. 11 are in a compressed logarithmic scale, which explains the reduced variation in amplitude. Finally, we computed the SNR_e of the inclusion under the two different experimental conditions of direction of electrode displacement, where the SNR_e values obtained are comparable. Comparing Figs. 10–12, it is apparent that for displacements at which there is a higher strain contrast and CNR_e, the corresponding SNR_e value is reduced slightly. However, this reduction in SNR_e does not discernibly affect the elastographic visualization of the inclusion.

Images from the second phantom are indicative of the fact that the electrode displacement method can be used with different electrode shapes and inclusion-background modulus contrasts. As stated earlier, the elastograms from the first phantom suffered from artifacts where the distal boundaries of the inclusion were not clearly visible [Fig. 2(a)]. This was hypothesized to be due to shadowing from the hooked end of the electrode. As expected, when the electrode used is a single straight cylindrical rod, these shadowing artifacts are not present. Note from Fig. 11(b) that the distal boundaries of the inclusion are continuous.

Both the TM phantoms constructed for evaluation of electrode displacement elastography had step changes in modulus between the inclusion and background. It is quite possible that in rf-ablated lesions the transition in modulus from the lesion to normal tissue is gradual rather than abrupt. Since it is extremely difficult to construct phantoms mimicking this gradual modulus transition, we instead tested our method on rf-ablated lesions created *in vitro* on canine liver tissue. The elastogram shown in Fig. 12(b) confirms that image quality comparable to that in phantoms can be obtained in real rf ablation experiments. It is premature to dwell on whether there is a "threshold" in modulus that is picked up by the algorithm on the elastogram; however, this is an interesting avenue for future research. It has been shown previously for external compression elastography that lesion size estimates compare favorably with pathology.[34] Additionally, manual and semiautomated segmentation have been shown to be accurate in delineating the lesion from surrounding normal tissue on elastograms.[58] We do not expect electrode displacement elastography to be any different. More extensive experiments on thermal lesion depiction within tissue specimens have been planned for electrode displacement elastography, but are beyond the scope of this article.

The results presented in this article serve to characterize the electrode displacement elastography technique over the displacement range studied, in terms of strain contrast, CNR_e, and SNR_e. It can be concluded that displacements at the higher end of the range studied resulted in marginally higher contrast and CNR_e. Also, the elastograms slightly underestimated the dimensions of the inclusion. This is possibly an inherent characteristic of the electrode displacement elastographic method, and needs further investigation. The method performed well for different electrode configurations and for both inclusion-background modulus contrasts studied. The images from the *in vitro* experiment also show that the method works in cases with possible gradual modulus transition patterns from lesion to normal tissue.

ACKNOWLEDGMENT

This work is supported by NIH Grant R01CA112192.

APPENDIX: CALCULATION OF THE CORRECTION FACTOR

Figure 13 (not to scale) shows the geometrical setup utilized to calculate the "correction factor" that is applied to the inclusion size estimates obtained from the strain images. As

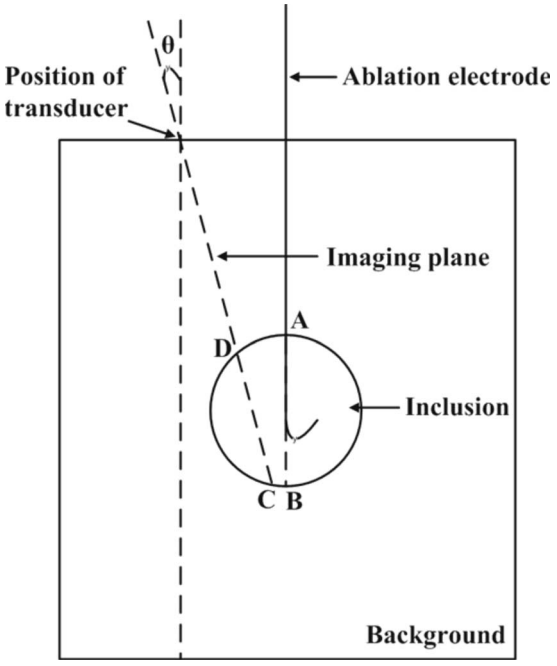

FIG. 13. Calculation of the "correction factor" used to account for inherent measurement errors in the inclusion size and area estimates.

stated earlier, since the plane imaged by the ultrasound transducer is slightly off-center with respect to the ablation electrode, the complete inclusion is not visualized. As a result, the size estimates (width, height, and area) are significantly less than the expected values (known values). To correct for this underestimation, we multiply the estimates by a correction factor to obtain corrected estimates.

The ultrasound transducer is placed at a distance of 12 mm from the ablation electrode (The thickness of the transducer prohibited its placement closer to the ablation electrode.) At this position, the transducer is held firmly at an angle of 10° with the vertical plane. This angle is represented by "θ" in Fig. 13. The plane imaged by the transducer is shown by the slanted dotted line in the figure. A segment of this line (segment *DC*) represents the plane of the inclusion that is imaged. Segment *AB* is the plane of the inclusion that represents its maximum two-dimensional size. For the inclusion width and height, the correction factor is defined to be the ratio of *AB* and *DC*. *AB* is the diameter of the inclusion and is known *a priori* to be 19 mm. From the geometry of the setup, *DC* is measured to be 16.5 mm. Hence, the correction factor by which the inclusion width and height estimates are multiplied is $19/16.5=1.1515$. The estimates for the inclusion area incorporate the variations in two dimensions and, as a result, the correction factor for the width and height is squared to obtain a new correction factor for the area estimates. Hence, the correction factor by which the area estimates are multiplied is given by $(AB/DC)^2=(1.1515)^2=1.326$. These corrected estimates are utilized to compare the estimated width, height, and area of the inclusion to the actual inclusion dimensions.

[a]Author to whom correspondence should be addressed. Telephone: (608)-265-8797; Fax: (608)-262-2413. Electronic mail: tvarghese@wisc.edu

[1]L. S. Wilson and D. E. Robinson, "Ultrasonic measurement of small displacements and deformations of tissue," Ultrason. Imaging **4**, 71–82 (1982).
[2]T. A. Krouskop, D. R. Dougherty, and F. S. Vinson, "A pulsed Doppler ultrasonic system for making noninvasive measurements of the mechanical properties of soft tissue," J. Rehabil. Res. Dev. **24**, 1–8 (1987).
[3]K. J. Parker, S. R. Huang, R. A. Musulin, and R. M. Lerner, "Tissue response to mechanical vibrations for 'sonoelasticity imaging'," Ultrasound Med. Biol. **16**, 241–246 (1990).
[4]Y. Yamakoshi, J. Sato, and T. Sato, "Ultrasonic imaging of internal vibration of soft tissue under forced vibration," IEEE Trans. Ultrason. Ferroelectr. Freq. Control **37**, 45–53 (1990).
[5]J. Ophir, I. Cespedes, H. Ponnekanti, Y. Yazdi, and X. Li, "Elastography: A quantitative method for imaging the elasticity of biological tissues," Ultrason. Imaging **13**, 111–134 (1991).
[6]T. Varghese, J. Ophir, E. Konofagou, F. Kallel, and R. Righetti, "Tradeoffs in elastographic imaging," Ultrason. Imaging **23**, 216–248 (2001).
[7]E. I. Cespedes, Ph.D. Dissertation thesis, University of Houston, 1993.
[8]M. Bertrand, M. Meunier, M. Doucet, and G. Ferland, "Ultrasonic biomechanical strain gauge based on speckle tracking," in IEEE Ultrasonics Symposium, (1989), pp. 859–864.
[9]M. O'Donnell, A. R. Skovoroda, B. M. Shapo, and S. Y. Emelianov, "Internal displacement and strain imaging using ultrasonic speckle tracking," IEEE Trans. Ultrason. Ferroelectr. Freq. Control **41**, 314–325 (1994).
[10]M. O'Donnell, A. R. Skovoroda, and B. M. Shapo, "Measurement of arterial wall motion using Fourier based speckle tracking algorithms," in Proceedings of the IEEE Ultrasonic Symposium (1991), 1101–1104.
[11]H. E. Talhami, L. S. Wilson, and M. L. Neale, "Spectral tissue strain: A new technique for imaging tissue strain using intravascular ultrasound," Ultrasound Med. Biol. **20**, 759–772 (1994).
[12]L. Gao, K. J. Parker, R. M. Lerner, and S. F. Levinson, "Imaging of the elastic properties of tissue—A review," Ultrasound Med. Biol. **22**, 959–977 (1996).
[13]K. Nightingale, M. Scott Soo, R. Nightingale, and G. Trahey, "Acoustic radiation force impulse imaging: In vivo demonstration of clinical feasibility," Ultrasound Med. Biol. **28**, 227–235 (2002).
[14]M. F. Insana, L. T. Cook, M. Bilgen, P. Chaturvedi, and Y. Zhu, "Maximum-likelihood approach to strain imaging using ultrasound," J. Acoust. Soc. Am. **107**, 1421–1434 (2000).
[15]Y. Zhu and T. J. Hall, "A modified block matching method for real-time freehand strain imaging," Ultrason. Imaging **24**, 161–176 (2002).
[16]A. F. van der Steen, C. L. de Korte, and E. I. Cespedes, "Intravascular ultrasound elastography," Ultraschall Med. **19**, 196–201 (1998).
[17]E. Konofagou and J. Ophir, "A new elastographic method for estimation and imaging of lateral displacements, lateral strains, corrected axial strains and Poisson's ratios in tissues," Ultrasound Med. Biol. **24**, 1183–1199 (1998).
[18]B. S. Garra, E. I. Cespedes, J. Ophir, S. R. Spratt, R. A. Zuurbier, C. M. Magnant, and M. F. Pennanen, "Elastography of breast lesions: Initial clinical results," Radiology **202**, 79–86 (1997).
[19]S. Y. Emelianov, X. Chen, M. O'Donnell, B. Knipp, D. Myers, T. W. Wakefield, and J. M. Rubin, "Triplex ultrasound: Elasticity imaging to age deep venous thrombosis," Ultrasound Med. Biol. **28**, 757–767 (2002).
[20]M. M. Doyley, J. C. Bamber, F. Fuechsel, and N. L. Bush, "A freehand elastographic imaging approach for clinical breast imaging: System development and performance evaluation," Ultrasound Med. Biol. **27**, 1347–1357 (2001).
[21]E. J. Chen, W. K. Jenkins, and W. D. O'Brien, Jr., "Performance of ultrasonic speckle tracking in various tissues," J. Acoust. Soc. Am. **98**, 1273–1278 (1995).
[22]W. F. Walker, F. J. Fernandez, and L. A. Negron, "A method of imaging viscoelastic parameters with acoustic radiation force," Phys. Med. Biol. **45**, 1437–1447 (2000).
[23]D. Melodelima, J. C. Bamber, F. A. Duck, J. A. Shipley, and L. Xu, "Elastography for breast cancer diagnosis using radiation force: System development and performance evaluation," Ultrasound Med. Biol. **32**, 387–396 (2006).
[24]D. Melodelima, J. C. Bamber, F. A. Duck, and J. A. Shipley, "Transient elastography using impulsive ultrasound radiation force: A preliminary

comparison with surface palpation elastography," Ultrasound Med. Biol. **33**, 959–969 (2007).
[25]J. Bercoff, M. Pernot, M. Tanter, and M. Fink, "Monitoring thermally-induced lesions with supersonic shear imaging," Ultrason. Imaging **26**, 71–84 (2004).
[26]J. L. Gennisson, M. Rénier, S. Catheline, C. Barriére, J. Bercoff, M. Tanter, and M. Fink, "Acoustoelasticity in soft solids: Assessment of the nonlinear shear modulus with the acoustic radiation force," J. Acoust. Soc. Am. **122**, 3211–3219 (2007).
[27]J. Ophir, B. Garra, F. Kallel, E. Konofagou, T. Krouskop, R. Righetti, and T. Varghese, "Elastographic imaging," Ultrasound Med. Biol. **26**, S23–S29 (2000).
[28]W. F. Walker, "Internal deformation of a uniform elastic solid by acoustic radiation force," J. Acoust. Soc. Am. **105**, 2508–2518 (1999).
[29]M. Fatemi and J. F. Greenleaf, "Application of radiation force in noncontact measurement of the elastic parameters," Ultrason. Imaging **21**, 147–154 (1999).
[30]K. R. Nightingale, R. W. Nightingale, M. L. Palmeri, and G. E. Trahey, "A finite element model of remote palpation of breast lesions using radiation force: Factors affecting tissue displacement," Ultrason. Imaging **22**, 35–54 (2000).
[31]A. P. Sarvazyan, O. V. Rudenko, S. D. Swanson, J. B. Fowlkes, and S. Y. Emelianov, "Shear wave elasticity imaging: A new ultrasonic technology of medical diagnostics," Ultrasound Med. Biol. **24**, 1419–1435 (1998).
[32]J. A. Ketterling and F. L. Lizzi, "Time-domain pressure response of arrays with periodic excitation," J. Acoust. Soc. Am. **114**, 48–51 (2003).
[33]T. Varghese, J. A. Zagzebski, and F. T. Lee, "Elastographic imaging of thermal lesions in the liver in vivo following radiofrequency ablation: Preliminary results," Ultrasound Med. Biol. **28**, 1467–1473 (2002).
[34]T. Varghese, U. Techavipoo, W. Liu, J. A. Zagzebski, Q. Chen, G. Frank, and F. T. Lee, Jr., "Elastographic measurement of the areas and volumes of thermal lesions resulting from radiofrequency ablation: Pathologic correlation," AJR, Am. J. Roentgenol. **181**, 701–707 (2003).
[35]E. Boctor, M. deOliveira, M. Choti, R. Ghanem, R. Taylor, G. Hager, and G. Fichtinger, "Ultrasound monitoring of tissue ablation via deformation model and shape priors," in *Medical Image Computing and Computer-Assisted Intervention*, Lecture Notes in Computer Science (Springer, Berlin, 2006), Vol. 4191, pp. 405–412.
[36]H. Ponnekanti, J. Ophir, and E. I. Cespedes, "Ultrasonic imaging of the stress distribution in elastic media due to an external compressor," Ultrasound Med. Biol. **20**, 27–33 (1994).
[37]T. Varghese, J. A. Zagzebski, and F. T. Lee, Jr., "Elastographic imaging of thermal lesions in the liver in vivo following radiofrequency ablation: Preliminary results," Ultrasound Med. Biol. **28**, 1467–1473 (2002b).
[38]R. J. Stafford, F. Kallel, R. E. Price, D. M. Cromeens, T. A. Krouskop, J. D. Hazle, and J. Ophir, "Elastographic imaging of thermal lesions in soft tissue: A preliminary study in vitro," Ultrasound Med. Biol. **24**, 1449–1458 (1998).
[39]T. Wu, J. P. Felmlee, J. F. Greenleaf, S. J. Riederer, and R. L. Ehman, "Assessment of thermal tissue ablation with MR elastography," Magn. Reson. Med. **45**, 80–87 (2001).
[40]R. Righetti, F. Kallel, R. J. Stafford, R. E. Price, T. A. Krouskop, J. D. Hazle, and J. Ophir, "Elastographic characterization of HIFU-induced lesions in canine livers," Ultrasound Med. Biol. **25**, 1099–1113 (1999).
[41]S. N. Goldberg, "Radiofrequency tumor ablation: Principles and techniques," Eur. J. Ultrasound **13**, 129–147 (2001).
[42]M. K. Jain and P. D. Wolf, "Temperature-controlled and constant-power radio-frequency ablation: What affects lesion growth?" IEEE Trans. Biomed. Eng. **46**, 1405–1412 (1999).
[43]A. Samali, C. I. Holmberg, L. Sistonen, and S. Orrenius, "Thermotolerance and cell death are distinct cellular responses to stress: Dependence on heat shock proteins," FEBS Lett. **461**, 306–310 (1999).
[44]P. Badini, P. De Cupis, G. Gerosa, and M. Giona, "Necrosis evolution during high-temperature hyperthermia through implanted heat sources," IEEE Trans. Biomed. Eng. **50**, 305–315 (2003).
[45]L. Solbiati, S. N. Goldberg, T. Ierace, T. Livraghi, F. Meloni, M. Dellanoce, S. Sironi, and G. S. Gazelle, "Hepatic metastases: Percutaneous radio-frequency ablation with cooled-tip electrodes," Radiology **205**, 367–373 (1997a).
[46]L. Solbiati, T. Ierace, S. N. Goldberg, S. Sironi, T. Livraghi, R. Fiocca, G. Servadio, G. Rizzatto, P. R. Mueller, A. Del Maschio, and G. S. Gazelle, "Percutaneous US-guided radio-frequency tissue ablation of liver metastases: Treatment and follow-up in 16 patients," Radiology **202**, 195–203 (1997b).
[47]L. Solbiati, T. Ierace, M. Tonolini, V. Osti, and L. Cova, "Radiofrequency thermal ablation of hepatic metastases," Eur. J. Ultrasound **13**, 149–158 (2001).
[48]S. N. Goldberg, G. S. Gazelle, L. Solbiati, T. Livraghi, K. K. Tanabe, P. F. Hahn, and P. R. Mueller, "Ablation of liver tumors using percutaneous RF therapy," AJR Am. J. Roentgenol. **170**, 1023–1028 (1998).
[49]F. Kallel, R. J. Stafford, R. E. Price, R. Righetti, J. Ophir, and J. D. Hazle, "The feasibility of elastographic visualization of HIFU-induced thermal lesions in soft tissues. Image-guided high-intensity focused ultrasound," Ultrasound Med. Biol. **25**, 641–647 (1999).
[50]J. Jiang, T. Varghese, Q. Chen, J. A. Zagzebski, and T. J. Hall, "Finite element analysis of tissue deformation with a radiofrequency ablation electrode for strain imaging," IEEE Trans. Ultrason. Ferroelectr. Freq. Control **54**, 281–289 (2007).
[51]E. L. Madsen, G. R. Frank, T. A. Krouskop, T. Varghese, F. Kallel, and J. Ophir, "Tissue-mimicking oil-in-gelatin emulsions for use in heterogeneous elastography phantoms," Ultrason. Imaging **25**, 17–38 (2003).
[52]E. L. Madsen, M. A. Hobson, H. Shi, T. Varghese, and G. R. Frank, "Tissue-mimicking agar/gelatin materials for use in heterogeneous elastography phantoms," Phys. Med. Biol. **50**, 5597–5618 (2005b).
[53]S. Y. Emelianov, J. M. Rubin, M. A. Lubinski, A. R. Skovoroda, and M. O'Donnell, "Elasticity imaging of the liver: Is a hemangioma hard or soft?" IEEE Ultrasonics Symposium Proceedings, Vol. 2, pp. 1749–1752 (1998).
[54]W. C. Yeh, P. C. Li, Y. M. Jeng, H. C. Hsu, P. L. Kuo, M. L. Li, P. M. Yang, and P. H. Lee, "Elastic modulus measurements of human liver and correlation with pathology," Ultrasound Med. Biol. **28**, 467–474 (2002).
[55]S. Bharat, U. Techavipoo, M. Z. Kiss, W. Liu, and T. Varghese, "Monitoring stiffness changes in lesions after radiofrequency ablation at different temperatures and durations of ablation," Ultrasound Med. Biol. **31**, 415–422 (2005).
[56]T. Varghese and J. Ophir, "An analysis of elastographic contrast-to-noise ratio," Ultrasound Med. Biol. **24**, 915–924 (1998).
[57]S. Srinivasan, J. Ophir, and S. K. Alam, "Theoretical derivation of SNR, CNR and spatial resolution for a local adaptive strain estimator for elastography," Ultrasound Med. Biol. **30**, 1185–1197 (2004).
[58]U. Techavipoo, T. Varghese, J. A. Zagzebski, Q. Chen, and W. Liu, "Semiautomated thermal lesion segmentation for three-dimensional elastographic imaging," Ultrasound Med. Biol. **30**, 655–664 (2004).